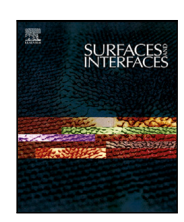
ELSEVIER

Contents lists available at ScienceDirect

Surfaces and Interfaces

journal homepage: www.sciencedirect.com/journal/surfaces-and-interfaces





Conservation of the robust ferromagnetic half-conductivity in 110-surface half-Heusler NaCrAs alloy by strains and defects

T.C. Chibueze a,b,*, A.T. Raji c, C.E. Ekuma d

- ^a Department of Physics & Astronomy, University of Nigeria, Nsukka 410001, Nigeria
- ^b Africa Centre of Excellence for Sustainable Power and Energy Development, University of Nigeria, Nsukka 410001, Nigeria
- c School of Computing, College of Science, Engineering and Technology (CSET), University of South Africa (UNISA), Florida 1709, South Africa
- ^d Department of Physics, Lehigh University, Bethlehem, PA 18015, USA

ARTICLE INFO

Keywords: Half-Heusler NaCrAs alloy Ferromagnetic half-conductivity Curie temperature Biaxial strain Surface phase diagram

ABSTRACT

We have studied the structural, electronic and magnetic properties of non-polar 110-surface of half-Heusler NaCrAs alloy (110-SHH NaCrAs) using the density functional theory and Korringa–Kohn–Rostoker Green's function method. Our results show that ferromagnetic half-conductivity (FHC) is exhibited by both the bulk and 110-SHH NaCrAs with a large spin-down energy gap of 2.61 eV and 1.70 eV respectively. The bulk high Curie temperature of 1223 K originates from the direct ferromagnetic exchange between nearest-neighbor (NN) Cr and As atoms as well as the Ruderman–Kittel–Kasuya–Yosida-type interaction between NN Cr atoms. Magnetic moment of 3.92 μ_B per formula unit was obtained for both the bulk and 110-SHH NaCrAs structures. We used biaxial strain to model the lattice mismatch between deposited thin film and the substrate. Our results reveal that FHC is retained in 110-SHH NaCrAs structure with -3% to 10% strain. Our phase diagram suggests that the 110-SHH NaCrAs composed of NaNaAs, NaCrNa, NaCrCr, CrCrAs, AsCrAs and NaAsAs can be synthesized under appropriate conditions. Additionally, electronic structure calculations show that the surface FHC is preserved only in NaNaAs, VcCrAs, CrCrAs, NaCrCr, NaVcAs and AsCrAs terminated surfaces. Overall, our results demonstrate that the half-Heusler NaCrAs alloy is a potential viable spin filter and spin source in spintronics devices.

1. Introduction

The quest for more compact and efficient digital devices has led to the integration of spin functionality into traditional electronics, giving rise to the field of spintronics. In spintronic devices, spin-polarized carriers are injected through a nonmagnetic metal, superconductor, nonmagnetic semiconductor or 2D electron gas channel barrier from a spin source into a drain layer. This introduction of spin-based functionality in electronics holds great promise for the future of technology and represents a significant area of current research [1]. Ferromagnetic half-conductors (FHCs) are a promising class of materials for efficient spin-polarized carrier transport due to their ability to allow only carriers with a specific spin state to cross the Fermi level, resulting in minimized spin-dependent scattering and ~100% spin polarization [2-7]. The discovery of FHCs in 1983 in the half-Heusler NiMnSb alloy [8] has sparked a significant amount of research on Heusler compounds, which are preferred over other materials such as metal oxides [9], ferrites [10,11], and perovskites [12] due to their high Curie temperature, large magnetic moments, and lattice constants that are well-matched

with those of relevant semiconductors for layered heterostructure fabrication [13–17]. Additionally, their properties can be easily tuned through defects, strains, and chemical compositions [18,19]. A major challenge with Heusler and half-Heusler compounds is that the FHC present in the bulk structure often disappears at the surfaces. However, recent theoretical investigations have shown that certain Heusler compounds such as $\rm Co_2MnSi$ [20], $\rm Co_2MnX$ (X = Si, Ge, Sn) [21], $\rm Ti_2FeSn$ [22] among others [23–26] exhibit FHC at the 100-surface while $\rm Co_2VAl$ [27], and $\rm Fe_2MnP$ [28] show FHC at specific surfaces and have a broader minority spin gap, which is less susceptible to the loss of FHC due to defects and thermal fluctuations.

Half-Heusler (HH) compounds, composed of a transition metal, an alkali metal/alkaline-earth metal, and a main group element, have recently gained attention in the field of spintronics due to their ability to exhibit ferromagnetic half-conductivity.[29–34] For example, recent studies have demonstrated mechanical stability and FHC in HH NaCrAs alloy (HH-NaCrAs) and other similar compounds [30,33,35]. However, their successful application as a spin filter or source in magnetic

^{*} Corresponding author at: Department of Physics & Astronomy, University of Nigeria, Nsukka 410001, Nigeria. E-mail address: timothy.chibueze@unn.edu.ng (T.C. Chibueze).

tunneling junctions (MTJs) requires the preservation of the FHC at the surface and interface with non-magnetic semiconductors. The 220-surface is the most prominent peak in the X-ray diffraction spectra of these compounds [36–40], and non-magnetic substrates like KCl(110) or MgO(110) have been proposed for deposition. However, the surfaces of deposited films are often imperfect and the lattice mismatch between half-Heusler compound and the semiconductor substrate leads to in-plane strain at the interface in MTJs. Therefore, a thorough understanding of how FHC in HH-NaCrAs responds to mechanical strain and defects is crucial for realizing its potential as a spin filter and spin source in spintronics.

In this paper, we investigate the electronic and magnetic properties of half-Heusler NaCrAs and explore its potential for spintronics applications. Specifically, we study ferromagnetic half-conductivity in the pristine 110-surface of HH-NaCrAs (110-SHH NaCrAs) and the effects of biaxial strain and surface point defects, including antisite and vacancy defects, on the FHC. We use *ab-initio* thermodynamics to construct a detailed phase diagram of the defect surface. Our results demonstrate that the FHC in 110-SHH NaCrAs remains even with biaxial strain and surface defects, highlighting its promise for spintronics.

2. Computational details

The properties of HH-NaCrAs were studied using first-principles density functional theory (DFT) as implemented in Quantum-ESPRESSO [41-44]. The exchange-correlation energy is approximated using the modified generalized gradient approximation of Perdew, Burke and Ernzerhof (PBEsol) [45]. The calculations were performed using a planewave basis set with a kinetic energy cut-off of 80 Ry and norm-conserving pseudopotentials [46]. The Monkhorst-Pack [47] method was used to sample the Brillouin zone for the bulk and 110surface structures, with $12 \times 12 \times 12$ and $12 \times 8 \times 1$ k-points, respectively. For these choice of k-points, the total energy is converged to 10^{-2} eV/atom. The bulk structure was modeled using the most stable β -phase primitive unit cell of the Cl_b crystal structure, space group F43 m (225). The non-polar 110-SHH NaCrAs was modeled using the bulk optimized lattice parameters with 1×1 cell size along the periodic a, b axes and a 45-atom (containing 15 NaCrAs formula units) stoichiometric symmetric slab that is non-periodic along c axis, with 17 Å vacuum separating the two faces.

Biaxial strain was simulated by applying strain simultaneously along the a and b axes, perpendicular to the 110 direction. Strains along a and b axes were applied from -10 to 10% in 1% increments. Two types of point defects were also considered, antisite defects and vacancies, in order to examine the effect of defects on FHC. All the atoms in both clean and disordered 110-SHH NaCrAs were fully relaxed while keeping only the three central atoms fixed. The spin polarization P was calculated for all the structures using the formula $P=(\mathrm{N}E_F^{\ 1}-\mathrm{N}E_F^{\ 1})\times 100\%$, where $\mathrm{N}_{E_F}^{\ 1,1}$ denotes the density of states at the Fermi level. The results of these calculations provide a deeper understanding of the behavior of FHC in HAH-NaCrAs under different conditions and can guide the design of spintronic devices using this material.

3. Results

3.1. Bulk and clean 110 surface

3.1.1. Structural and phonon properties

We obtained and optimized lattice constant of 6.28 Å for bulk HH-NaCrAs (see Figure S1(a) [48]), which is numerically the same as the value of 6.36 Å reported by Rostami [30]. The slight difference may be due to different functional we used in our calculations. We also modeled the 110-SHH NaCrAs from the optimized bulk structure as shown in Figure S1(b) [48]. Our calculations led to a lattice parameter of 4.44 Å and 6.28 Å in the **a** and **b** directions, respectively. The

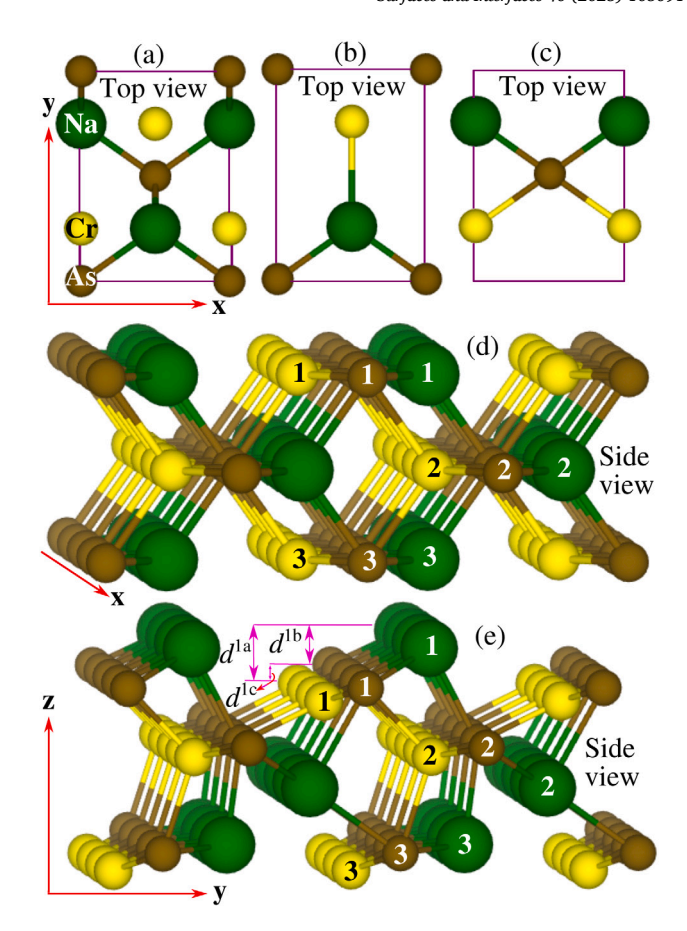


Fig. 1. The crystal structure of 110 surface of half-Heusler NaCrAs alloy (space group $F\bar{4}3$ m) (a) Top view of the entire slab (b) Top view of only the surface layer (c) Top view of only the sub-surface layer (d) Side view of the first three top layers of the unrelaxed structure (e) Side view of the first three top layers of the relaxed structure. The atoms labeled '1', '2' and '3' denote atoms in the first, second and third layers respectively.

structure of the 110-SHH NaCrAs consists of two alternating NACrAs layers with specific atom placement, as shown in Figs. 1(a–c). After full relaxation of the slab, significant changes were observed in the surface structure, as seen in Fig. 1(e). All the atoms except the atoms around the middle of the slab were displaced along the c-direction. The vertical distance between Na(Cr) and As in the surface layer (A-layer) is 0.97 Å (0.42 Å), increasing (decreasing) the length of the Na-As (Cr-As) bond from 2.72 Å to 3.01 Å (2.47 Å). Also, vertical distance between Na and Cr atoms at the surface is 1.39 Å . The pattern of atomic displacement decreases from the surface to the center of the slab, with no displacement in the 7th layer, indicating that the slab size is sufficient.

We calculated the lattice dynamical properties of the bulk HH-NaCrAs alloy using the density functional linear response theory [49, 50], and $4\times4\times4$ q-mesh in the Brillouin zone; our result is presented in Fig. 2. The calculated full zone phonon dispersion and atomic projected phonon density of states do not incorporate negative frequencies signifying that HH-NaCrAs is dynamically stable in the β -phase. The phonon spectra display three acoustical branches and six optical branches which is consistent with the three atoms contained in the primitive unit cell of HH-NaCrAs. Each of the two distinct optical modes region as well as the acoustical branch in the spectra is threefold degenerate at the zone center. The Na atom contributes significantly to the distinct high frequency (~240 cm^-1) optical phonon modes, Cr atom contributes most to the optical mode around 150 cm^-1 while the As atom with highest atomic mass contributes majorly to the

Table 1 Vertical intra/inter layer distance between Na and As $(d_{\text{Na-As}})$, Cr and As $(d_{\text{Cr-As}})$, Na and Cr $(d_{\text{Na-Cr}})$ in half-Heusler NaCrAs 110 surface slab; atomic magnetic moment of Na (M_{Na}) , Cr (M_{Cr}) , As (M_{As}) , total magnetic moment per layer and bulk (M_{Total}) .

Layer/	$d_{\text{Na-As}}$	$d_{\text{Cr-As}}$	$d_{\text{Na-Cr}}$	$M_{ m Na}$	M_{Cr}	M_{As}	M_{Tot}
bulk	(Å)	(Å)	(Å)	(μ_B)	(μ_B)	(μ_B)	(μ_B)
1st	0.97	0.42	1.39	0.03	4.08	-0.35	3.77
2nd	1.14	0.31	0.84	0.05	3.90	-0.32	3.63
3rd	0.15	0.52	0.87	0.04	4.41	-0.27	4.18
4th	0.12	0.48	0.17	0.04	4.31	-0.29	4.06
7th	0.00	0.00	0.00	0.03	4.21	-0.33	3.91
Bulk				0.03	4.22	-0.33	3.92
					3.80 ^a	-0.23^{a}	4.00 ^a
					3.73^{b}	-0.18^{b}	4.00^{b}
1st - 2nd	2.47	1.80	2.78				
2nd - 3rd	2.71	2.55	2.24				
3rd - 4th	2.41	1.74	2.36				

aRef.[30].

^bRef.[35].

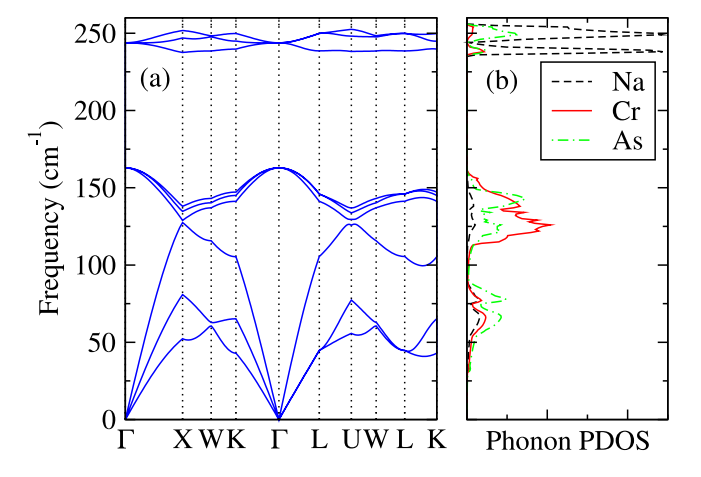


Fig. 2. Full zone phonon dispersion relation along the high symmetry points in the Brillouin zone (b) Atomic projected phonon density of states of HH-NaCrAs alloy in the β -phase.

transverse acoustical modes around frequency of 75 cm⁻¹. The phonon dynamical stability of HH-NaCrAs alloy lends considerable credence to the stability and synthesizability of the half-Heusler phase.

3.1.2. Electronic properties

To better understand the physical properties of HH-NaCrAs, we calculated the electronic band structure, the density of states, and the atomic projected density of states of the bulk as well as that of the 110-surface. Our calculations show that bulk NaCrAs is ferromagnetic with metallic spin-up channel and an energy band gap, E, of ~ 2.61 eV in the spin minority channel (Fig. 3(a) & (b)). From the electronic band structure, we observe that the spin minority E_{σ} is indirect along the X – L of the high symmetry zone with the Cr-d split into triply degenerate t_{2g} (d_{xy}, d_{xz}) and d_{yz} and doubly degenerate e_g $(d_{x^2-y^2})$ and d_{z^2} suborbitals. The atomic projected density of states (Fig. 3(c)) show that there is strong hybridization between the As-p and Cr-d orbitals. From the analysis of the electronic structure, the we observe that there is strong hybridization between the As-p orbital and the Cr-t2g sub-orbital to form a triply degenerate *p*-like bonding states and a triply degenerate antibonding states, resulting to energy gap in the spin-down electronic states. The 4p and 4s orbitals are filled as a result of apparent charge transfer from the Cr- t_{2g} orbitals, leading to covalent bond between them and leaving only the spin-up orbitals of the $Cr-e_{\sigma}$ filled. This view is further expressed by the charge density difference plot shown in Figure S2. The primitive unit cell of the HH-NaCrAs therefore contains total of eight occupied spin-up states and four occupied spin-down

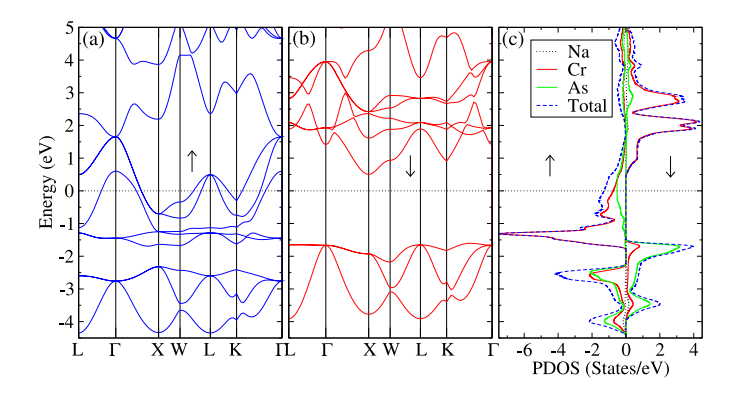


Fig. 3. Electronic properties of bulk half-Heusler NaCrAs alloy (a) electronic energy structure for the spin-up states (b) electronic energy structure for spin-down states (c) density of states projected on the atomic orbitals where the dotted black line, continuous red line, and continuous green line represent the atomic orbitals of Na, Cr and As respectively while the dotted blue line represent the total density of states of the bulk structure. The left panel of (c) is the spin-up states while the right is the spin-down. The horizontal dotted line denote the Fermi level. (For interpretation of the references to color in this figure legend, the reader is referred to the web version of this article.)

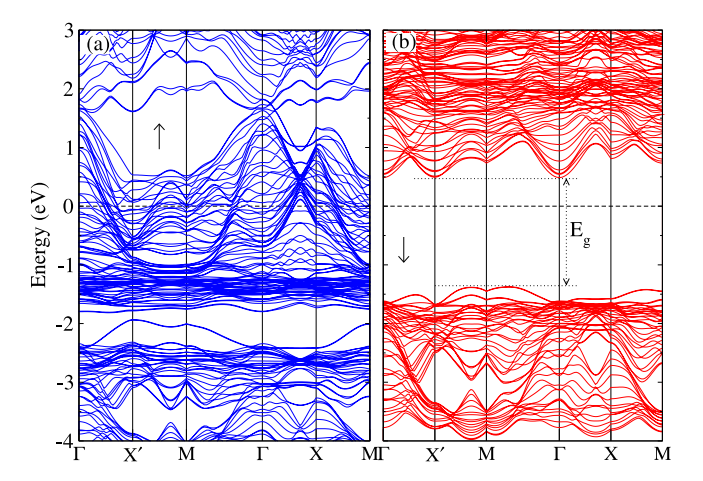


Fig. 4. Electronic structure of clean 110-surface of half-Heusler NaCrAs alloy (a) spin-up states (b) spin-down states. The horizontal dotted line denote the Fermi level.

states. This predicts magnetic moment of $4\mu_B/{\rm fu}$ in accordance with the amended Slater-Pauling rule, $M_{\rm tot}=N_{\rm v}-8$ [51], where $M_{\rm tot}$ and $N_{\rm v}$ are the magnetic moment and valence electron content per formula unit respectively. Figs. 4 and 5 depict the calculated electronic structure of 110-SHH NaCrAs. Our calculations show a metallic solution in the spin-majority channel with semiconducting behavior characterized by an indirect $E_{\rm g} \sim 1.71$ eV along the Γ and X' in the spin-minority channel. Our calculated data show that the difference between the bulk and surface minority spin gap is primarily caused by states belonging to the first and second layer of Na and As atoms (Fig. 5(a)&(c)).

3.1.3. Magnetic moments and exchange parameters

We conducted a detailed analysis of the magnetic properties of HH-NaCrAs alloy by computing the magnetic moment of the bulk and 110 surface as well as the exchange parameters of the bulk (Table 1). The Cr atoms were found to be the dominant contributors to the magnetic moment in both the bulk and 110 surface structures, while the contribution from the Na atoms was found to be negligible. However, the magnetic moment of the As atoms was found to be antialigned with that of the Cr and Na atoms. Our result for the bulk is largely in agreement with other theoretical results [30,35] performed with different exchange—correlation functional. When considering the

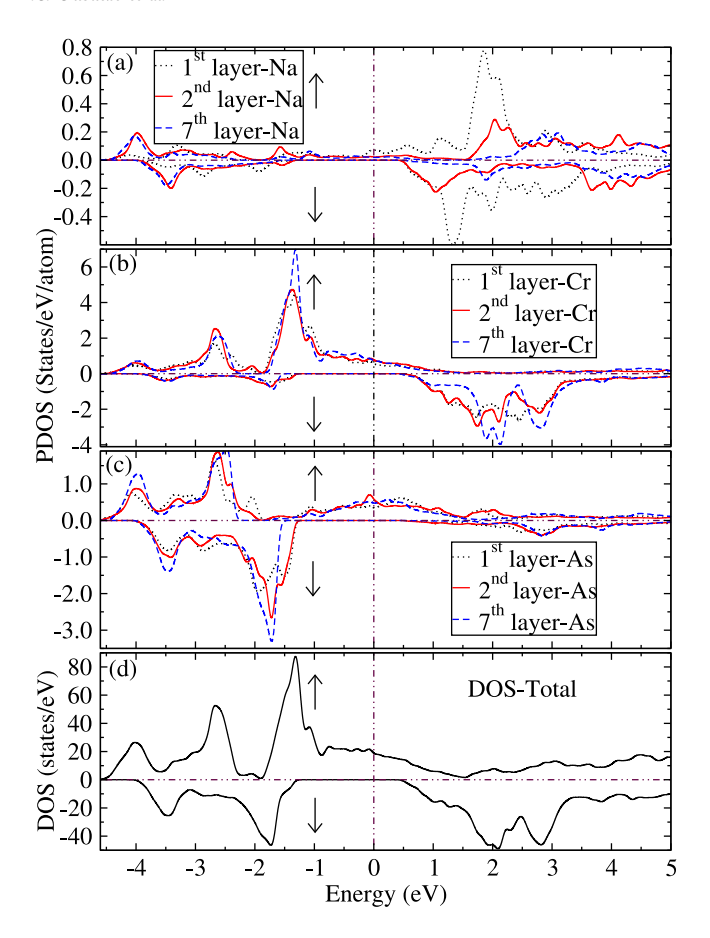


Fig. 5. Density of states projected (PDOS) on (a) Na atomic orbitals (b) Cr atomic orbitals (c) As atomic orbitals of the 110-surface of half-Heusler NaCrAs alloy (110-SHH NaCrAs). We have presented only atoms in the first, second and seventh layers (d) Total density of states (DOS) of 110-SHH NaCrAs. The upper panel of each subfigure is the spin-up while the lower panel is the spin-down. The vertical dotted line across the Figure denote the Fermi level.

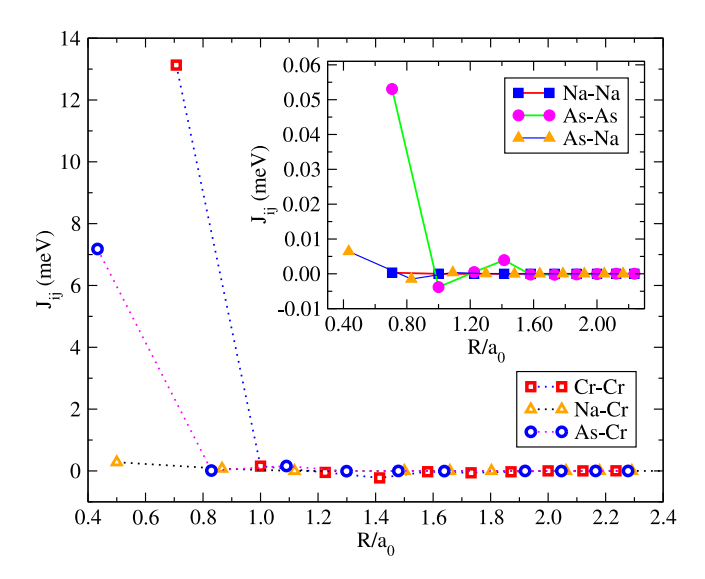


Fig. 6. Dependence of magnetic exchange parameter on the distance between the atoms normalized by the lattice constant of the bulk half-Heusler NaGrAs alloy.

surface layer, a notable trend was observed where the total magnetic moment per layer increases from the first layer, peaks in the third layer, and then decreases to the value of the bulk magnetic moment per formula unit. In the second layer, a similar pattern was observed. These findings support the conclusion that the 110-SHH NaCrAs sample is sufficiently large to accurately reflect the magnetic properties of the bulk structure around the center of the slab.

In addition to calculating the magnetic moments, we also calculated the exchange parameters in order to study the magnetic interaction. This was accomplished using the spin-polarized scalar-relativistic potential mode within the Green's function-based Korringa-Kohn-Rostoker (KKR) approach [52,53]. We employed the generalized gradient approximation to parametrize the exchange-correlation potential. The KKR muffin-tin radii for Na, Cr, and As were set at 2.02, 1.44, and 1.52 Å, respectively. A dense and evenly distributed grid with 1000 points was used to sample the irreducible Brillouin zone, and a 30-point mesh on the energy plane was used to evaluate the energy integral along a semicircular path. The angular momentum expansion cutoff was set at 3 for the multipole expansion of the Green's function. We note that due to the computational complexity of the Green's function approach, it is not feasible to apply it to the surface structures. However, since our optimal surface termination is known to have similar electronic and magnetic properties as the bulk, we can assert that the magnetic exchange interactions reported for the bulk can provide useful insights into the magnetic properties of the surface. Within the Heisenberg model, the magnetic exchange interaction is [54,55]

$$\hat{\mathcal{H}} = -2\sum_{i>j} J_{ij} \mathbf{S}_i \mathbf{S}_j,\tag{1}$$

where J_{ij} is the exchange interaction between spin moments on atoms with unit vector S_i and S_j located at i and j, respectively. The spatial-dependent magnetic exchange constant J_{ij} is estimated as [56],

$$J_{ij} = \frac{1}{4\pi} \int_{-E_F}^{E_F} dE \ tr(\Lambda_i \hat{Y}_{\uparrow}^{ij} \Lambda_j \hat{Y}_{\downarrow}^{ji}), \tag{2}$$

where $\Lambda_{i(j)} = t_{i(j)\uparrow}^{-1} - t_{i(j)\downarrow}^{-1}$, $t_{\uparrow(\downarrow)}^{-1}$ is the differential in inverse of the scattering t-matrix of the magnetic species at various sites for the spin channels, $\hat{Y}_{\uparrow(\downarrow)}^{ij}$ is the scattering path operator between i and j sites for the ground state, and tr is the trace over the orbital components of the scattering matrices. We calculated the exchange parameter by assuming that a Cr atom is at the center of a cluster of radius $R^{c=max,|R_i-R_j|} \sim 4.50$ Å, as presented in Fig. 6. Our results indicate that the most significant exchange interactions occur between neighboring Cr and As atoms, with $Jij^0 \sim 7.18$ meV and between nearest neighbor Cr atoms, $Jij^0 \sim 13.13$ meV. However, when the Cr and As atoms are not immediate neighbors, the exchange interaction between them becomes negligible.

Our results suggest that the Cr-As exchange is a direct exchange interaction, which is mediated by the overlap of their electronic wavefunctions. However, the large distance between nearest neighbor (NN) Cr atoms (4.44 Å) does not allow for direct exchange between them. Instead, the NN Cr atoms are able to interact via mediation by conduction electrons from As and Na atoms, which results in a large magnitude of exchange interaction similar to the Ruderman-Kittel-Kasuya-Yosida (RKKY) interaction. As our analysis has shown, this RKKY interaction is only significant between the nearest neighbor Cr atoms, and quickly diminishes beyond them. This could be attributed to the substantial localization of the As electrons and ferromagnetic coupling between the atoms (as seen in the inset of Fig. 6) as well as the limited number of conduction electrons provided by the Na atoms. The small magnetic moments observed on the Na and As atoms are the result of the spin-polarization of their conduction electrons. Using the computed exchange interaction parameter, we compute the Curie temperature (T_C) within the mean-field approximation by obtaining the largest eigenvalue of $(\Omega - TI)\rho = 0$, which is an eigenvalue matrix representation of the coupled mean-field approximation as [54]

$$\kappa_B T_C \langle \mathbf{S}_i \rangle = \frac{2}{3} \sum_j J_{ij}^0 \langle \mathbf{S}_j \rangle, \tag{3}$$

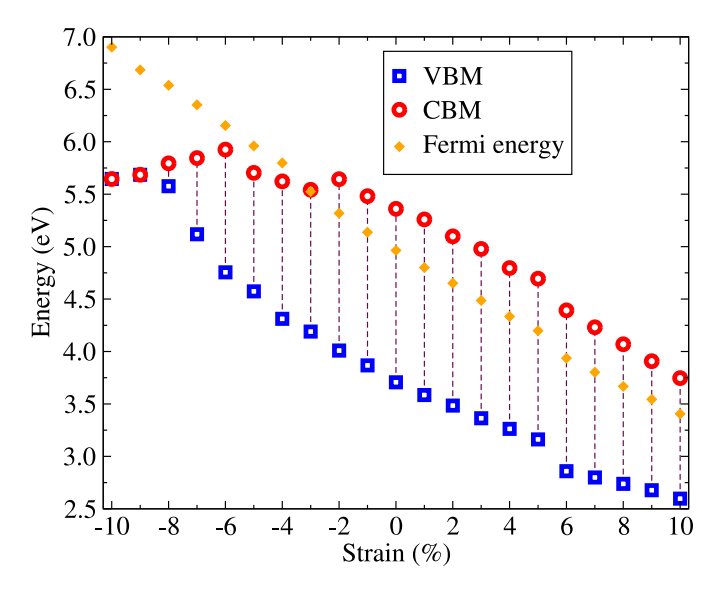


Fig. 7. Variation of the energy of valence band maximum (VBM), conduction band minimum (CBM), and the Fermi level with biaxial strain in the 110-surface of half-Heusler NaCrAs alloy spin-down electronic structure. Negative (positive) values of the strain depict compressive (tensile) biaxial strain. The energy difference between the CBM and VBM for a value of strain is the spin-down energy band gap of the corresponding value of strain. Note that below -3% strain, the Fermi level shifts outside the VBM-CBM gap and the ferromagnetic half-conductivity is destroyed.

where **I** is a unit matrix, $\Omega_{ij} = (2/3)k_BJ_{ij}^0$, ϱ is the matrix representation of $\langle \mathbf{S}_j \rangle$, κ_B is the Boltzmann constant, and $\langle \mathbf{S}_j \rangle$ is the average projection of \mathbf{S}_j in the z direction. We also note that the MFA overestimates the Curie temperature due to some excluded magnetic effects [57,58]. The calculated Curie temperature is 1223 K, which is significantly above room temperature, making it a highly viable material for spintronic applications. The high Curie temperature ensures that the magnetic properties of the material remain stable even at elevated temperatures, which is essential for the proper functioning of spintronic devices. Additionally, having a Curie temperature above room temperature also means that the material can be used in a wide range of environments and conditions without losing its magnetic properties, which further increases its potential for practical applications in spintronics. Unfortunately, we do not have any experimental data to correlate our results with.

3.2. Biaxial strain in 110 surface

It is important to study the effects of strain on layer-by-layer deposition of thin films as it can have a significant impact on the electronic and magnetic properties of the material. To investigate this, we modeled the strains inherent in layer-by-layer deposition of thin film due to lattice mismatch between the film and the substrate by applying biaxial strain on the two periodic sides of the 110-SHH NaCrAs. During our structural optimization, all the atoms in the 110 surface were allowed to fully relax upon application of the strain, in order to simulate the epitaxial strain inherent in deposited films. The results of this analysis are presented in Fig. 7. The details of the electronic density of states and the atomic projected density of states of the strained structures are presented in the Supplemental Materials (Figure S3 and S4) [48]. We found that the FHC in 110-SHH NaCrAs is retained up to a compressive strain of -3%, beyond which it is lost. Conversely, the FHC is retained for all values of tensile strain studied, which suggests that the HH-NaCrAs alloy is more compelling for spintronic applications when deposited on a substrate with a slightly higher lattice constant. We observed that the energy of the valence band maximum (VBM) and conduction band minimum (CBM) of 110-SHH NaCrAs both increased with tensile strain

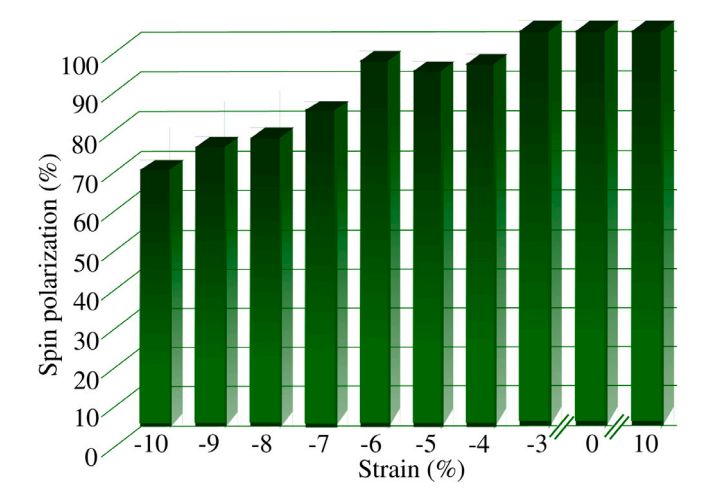


Fig. 8. Dependence of spin polarization of half-Heusler NaCrAs alloy 110-surface on biaxial strain. Negative (positive) values of the strain depict compressive (tensile) biaxial strain.

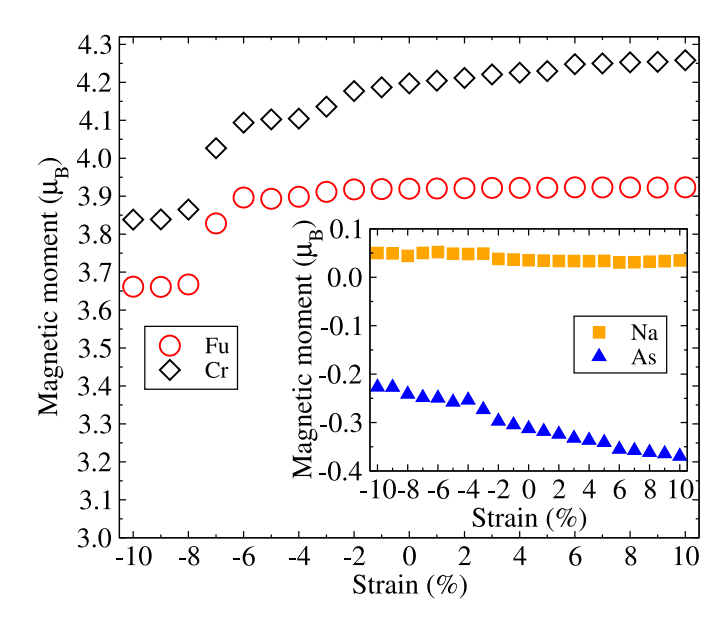


Fig. 9. Variation of the average magnetic moment of Na atoms, Cr atoms, As atoms, and the per NaCrAs formula unit (FU) of 110-surface half-Heusler NaCrAs alloy with biaxial strain. Negative (positive) values of the strain depict compressive (tensile) biaxial strain.

and decreased with compressive strain. The Fermi energy also increased with tensile strain and decreased with compressive strain. Both the VBM and CBM increased at about the same rate, thus keeping the spin-minority energy band gap of the 110-SHH NaCrAs almost constant between 10 and -2% strain. The application of compressive strain lifts the degenerate energy states, which pushes the Fermi level to higher energies. This results in some finite states appearing around the Fermi level in the spin-down component. High values of compressive strain completely lift the degeneracy in the Cr-d states, which in turn lowers the spin configuration of these states by partially filling the spin-down Cr-d states.

The results of our spin polarization calculations for various strains on 110-SHH NaCrAs are presented in Fig. 8. We found that between a strain of 10 and -3%, the material maintains 100% spin polarization. However, at $\sim -4\%$ strain, the spin polarization drops to $\sim 92\%$, and then slightly increased to $\sim 93\%$ at -6% strain before decreasing continuously to $\sim 66\%$ at -10% strain. Notably, even at a strain of -9%, the material still retains a spin polarization as high as 74%. The response

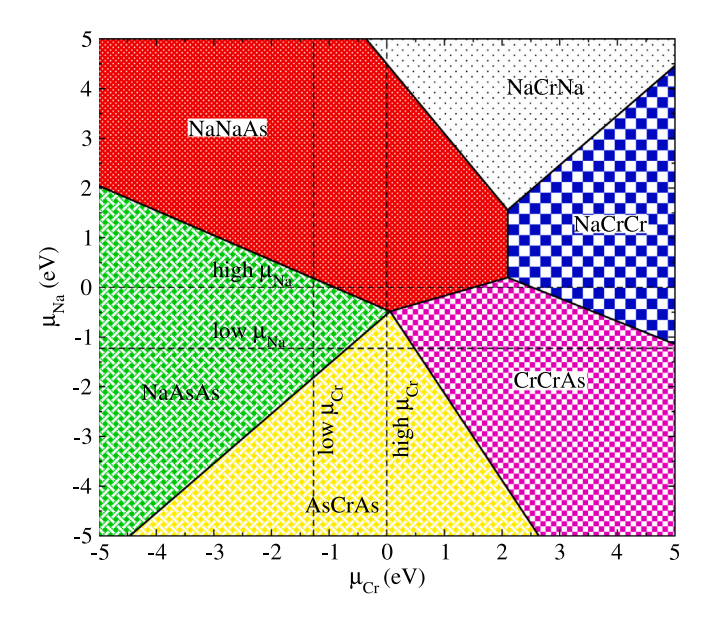


Fig. 10. Phase diagram of half-Heusler NaCrAs alloy 110-surface with respect to the various surface compositions represented by various color shadings, NaNaAs connote a surface with Na at Cr site; NaCrNa connote a surface with Na at As site; NaCrCr connote a surface with Cr at As site; CrCrAs connote a surface with Cr at Na site; AsCrAs connote a surface with As at Na site: NaAsAs connote a surface with As at Cr site. The dashed lines depict the upper and lower limits of the Na chemical potential (μ_{Na}) and Cr chemical potential (μ_{Cr}) .

of the magnetic moment to biaxial strain is presented in Fig. 9. We observed that tensile strain increases the distance between the atoms and reduces the magnetic interaction between them, allowing each atomic species to exhibit a magnetic moment much closer to that of the isolated atom. The average magnetic moment of Na atoms increases gently but continuously from 10% to -10% strain. The average magnetic moment per atom of Cr decreases gradually from 10% to -7% strain. Similarly to the average magnetic moment of Na atoms, the average magnetic moment per atom of As increases progressively but with a higher gradient from 10% to -10% strain. The overall effect is that the average magnetic moment per formula unit of 110-SHH NaCrAs remains constant between 10 and -3% strain and decreases discontinuously between -6 and -8% strain. The discontinuity in the decrease of magnetic moment per formula unit in 110-SHH NaCrAs suggests a transition from high-spin to low-spin Cr-d configuration. For example, the magnetic moment of the eighth layer Cr atom at -7%and -8% strains are 3.84 μ_B and 3.14 μ_B , respectively, while that of the first layer remains at $\sim 4.0 \ \mu_B$ at both strains. Our interpretation is that compressive biaxial strain ($\leq -8\%$) transforms the half-Heusler tetrahedral field to square planar field and lifts the degenerate energy states in the Cr-d orbital leading to a low-spin configuration of the d orbital.

3.3. Point defects on 110 surface

In this section, we investigated the effects of point defects on the electronic and magnetic properties of 110-SHH NaCrAs, which often occur during thin film deposition. To model these defects, we substituted one atom with another atom of the same compound or created a vacancy at the surface by removing an atom without replacement. In our model, for example, we referred to the structure with Cr atoms replaced by Na atoms as NaNaAs, and the structure with a Na vacancy as VcCrAs, where Vc denotes a vacancy. We studied a total of nine different defect structures, each with only one defect at the surface while maintaining the slab's symmetry.

We employed ab-initio thermodynamics [59] to map the phase diagram of different surface compositions of 110-SHH NaCrAs when

Strain and defect modeling in half-Heusler NaCrAs. MM_{No.2} MM_{Cr} and MM_{As} symbolize magnetic moment of the surface layer Na, Cr and As atoms respectively in 110-SHH NaCrAs with surface point defects. The symbol "#" is used to label magnetic moment

atoms in antisite positions. MM_{E_0} and P symbolize the magnetic moment per formula unit and spin polarization of defect structures respectively while E_{α} connote the energy band gap in the spin-down electronic structure. Vc is used to represent a vacant site.

buna gap m	the spin down	r creetronic on	detailer ve io t	accurate repri	cociii a vac	une orec.
Defect	MM_{Na}^{1st}	MM_{Cr}^{1st}	MM_{As}^{1st}	MM_{Fu}	$E_{\rm g}$	\boldsymbol{P}
structure	(μ_B)	(μ_B)	(μ_B)	(μ_B)	(eV)	(%)
NaCrAs	0.033	4.079	-0.319	3.920	1.71	100
NaNaAs	0.031		-0.311	3.264	1.16	100
	0.023^{\sharp}					
NaCrNa	0.034	4.898		4.116	0.00	85
	0.008^{\sharp}					
VcCrAs		3.857	-0.512	3.792	1.25	100
CrCrAs		3.535	-0.319	3.268	0.34	97
		-2.500^{\sharp}				
NaCrCr	-0.035	3.917		3.527	0.51	100
		-0.163^{\sharp}				
NaVcAs	0.006		-0.343	3.136	1.05	100
AsCrAs		3.230	-0.168	3.658	0.48	100
			-0.243^{\sharp}			
NaAsAs	0.013		-0.164	3.444	0.00	87
			0.128^{\sharp}			
NaCrVc	-0.068	4.889		4.086	0.00	84

they have bulk HH-NaCrAs as a thermodynamic reservoir. The surface free energy (γ) of symmetric 110-SHH NaCrAs is obtained as

$$\gamma(T,p) = \frac{1}{A} [G_{\text{NaCrAs}}^{\text{slab}}(T,p,N_i) - \sum_i N_i \mu_i(T,p)], \tag{4}$$

where A, $G_{\mathrm{NaCrAs}}^{\mathrm{slab}}$, N_i , and μ_i denote the total area of the slab surface perpendicular to the growth direction, Gibbs free energy of 110-SHH NaCrAs, number and chemical potential of i atoms in the 110-SHH NaCrAs respectively; i denote Na, Cr and As elements. Since experimental conditions affect the surface free energy and surface stability via the chemical potentials, we express the surface free energy in terms of the chemical potential of Na and Cr only since they crystallize out more readily in experiments than As. The chemical potentials of Na and Cr are related by

$$\mu_{\text{Na}} + \mu_{\text{Cr}} + \mu_{\text{As}} = G_{\text{NaCrAs}}^{\text{bulk}},\tag{5}$$

if the slab is in thermodynamic equilibrium with the bulk HH-NaCrAs alloy, where $G_{\mathrm{NaCrAs}}^{bulk}$ is the Gibbs free energy of the bulk HH-NaCrAs. Combining Eqs. (4) and (5) and eliminating μ_{As} gives

$$\begin{split} \gamma(T,p) &= \frac{1}{A} [G_{\text{NaCrAs}}^{\text{slab}}(T,p,N_i) - N_{\text{Na}} \mu_{\text{Na}} - N_{\text{Cr}} \mu_{\text{Cr}}] \\ &- N_{\text{As}} [G_{\text{NaCrAs}}^{\text{bulk}} - \mu_{\text{Na}} - \mu_{\text{Cr}}], \end{split} \tag{6}$$

where the surface compositions with lower $\gamma(T, p)$ are more stable. The lower limit of $\mu_{\rm Na}$ is given by $G_{\rm NaCrAs}^{\rm bulk} - G_{\rm CrAs}^{\rm bulk}$ while the upper limit is the Gibbs free energy of bulk hcp-Na. The lower limit of μ_{Cr} is determined by the difference between the Gibbs free energy of bulk NaCrAs and bulk NaAs, while the upper limit is the Gibbs free energy of bulk bcc-Cr. Below the lower limit of μ_{Na} (μ_{Cr}), Na (Cr) will crystallize out of the slab, forming CrAs (NaAs) compound. However, under certain experimental conditions, regions of the phase diagram outside these limits can be realized. In our calculations, we assumed that the net vibrational contribution to $\gamma(T, p)$ is zero and used DFT total energy differences alone. Our result of the phase diagram, presented in Fig. 10, includes six different surface terminations. The phase diagram shows that NaAsAs, AsNaAs, NaNaAs and CrCrAs are the most attainable surface compositions of the defect structures. It is worth noting from the phase diagram that under As-rich conditions, NaCrNa and NaCrCr surface compositions can also be realized. All the surfaces with vacancies are missing in the phase diagram, possibly due to the higher energy required to create these vacancies relative to the other defects.

To understand the electronic properties of the surface defect structures, we examined their various density of states (DOS) and partial density of states (PDOS); our results are presented in Table 2. Further details of the DOS and PDOS are presented in Figures S5-S10 [48]. Of the defect structures that appear in the phase diagram, the NaNaAs, NaCrCr, and AsCrAs surface compositions have 100% spin polarization, with spin-down energy band gaps of 1.16 eV, 0.51 eV, and 0.48 eV, respectively. The NaCrNa, CrCrAs, and NaAsAs surface compositions have very high spin polarizations of 85%, 97%, and 87%, respectively. With respect to the three compositions with vacancies, the VcCrAs and NaVcAs exhibit 100% spin polarization with minority spin gaps of 1.25 eV and 1.05 eV, respectively, while NaCrVc exhibits 84% spin polarization. Out of the nine different surface defect structures considered in this work, six exhibit ferromagnetic half-metal characteristics while four out of the six with FHC appear in the phase diagram. The loss of FHC in some of these structures is due to the presence of antisite atoms or vacancies at the surface which disrupt the Cr-As hybridization. The loss of FHC in NaCrNa is as a result of spin-down electronic states originating from the first and second layer atoms crossing the Fermi level which are stimulated by the presence of antisite Na atom in the As site. In NaAsAs, FHC is destroyed by spin-down electronic states originating from the Na in the first and second layer as well as the two As atoms in the first layer. In NaCrVc, the loss of FHC is due to spin-down states originating from Na and Cr in the first layer as well as Na and As in the second layer. In all the defect structures where FHC is lost, the Cr-As hybridization is interrupted either by an antisite atom or vacancy at the surface.

The magnetic properties of the various defects are revealed by analyzing their magnetic moments (see Table 2). In our discussions, we refer to the surface atomic moment (surface atom) as simply atomic moment (atom). The magnetic moment per formula unit (MMFu) of NaVcAs is much smaller than that of the clean slab due to the vacancy created by the missing Cr atom, which has a dominant magnetic moment. The same reason applies to the lower $\mbox{MM}_{\mbox{\scriptsize Fu}}$ of NaNaAs and NaAsAs where the Cr atom has been substituted by Na and As, respectively. Similarly, all the Cr atoms in antisite position in CrCrAs and NaCrCr are antiferromagnetically aligned to the Cr atom in the normal Cr site, resulting in smaller MM_{Fu} in comparison with that of the defect-free surface. In NaCrVc and NaCrCr where the As site is vacant or substituted by a Cr atom, the Na atom becomes antiferromagnetically aligned to the Cr atom, unlike the case in the defect-free surface where they are ferromagnetically aligned. The As atom in the Cr site is antiferromagnetically aligned to the As atom in the normal site. It is noteworthy that MM_{En} of the surface defect compositions that exhibit 100% spin polarization are less than that of the clean slab while the defects with MMFu greater than that of the clean slabs have spin polarization below 100%.

4. Conclusions

In conclusion, we have studied the structural, phonon, electronic, and magnetic properties of the bulk and 110-surface of the half-Heusler NaCrAs alloy using ab-initio methods. Our results indicate that the dynamically stable bulk structure has a lattice constant of 6.28 Å and the symmetric non-polar 110-surface structure exhibits relative vertical displacement among the surface atoms upon relaxation. Both the bulk and surface structures exhibit ferromagnetic half-conductivity with large electronic energy band gaps of 2.16 eV and 1.70 eV, respectively. We also investigated the magnetic exchange interaction in the bulk structure and found significant ferromagnetic direct exchange interaction between nearest neighbor Cr and As atoms, as well as Ruderman-Kittel-Kasuya-Yosida interaction pattern between nearest neighbor Cr atoms enhanced by conduction electrons from As and Na atoms. Using a mean-field approximation, we obtained a HH-NaCrAs Curie temperature of ~1223 K. The magnetic properties of the bulk and 110-SHH NaCrAs show a magnetic moment per formula unit of 3.92 μ_B ,

with a significant portion of the magnetic moment residing on the Cr atoms. We also examined the robustness of the 110-SHH NaCrAs FHC by subjecting the structure to biaxial strains and point defects on the surface. Our results showed that the FHC is preserved up to 10 to -3% strains and the FHC is preserved in six out of the nine different defect structures. This study provides a comprehensive understanding of the electronic and magnetic properties of the bulk and 110-SHH NaCrAs alloy, which can be useful in the design and development of spintronic devices.

CRediT authorship contribution statement

T.C. Chibueze: Conceptualization, Methodology, Writing – original draft, Software, Formal analysis. **A.T. Raji:** Writing – review & editing, Data curation, Resources. **C.E. Ekuma:** Supervision, Software, Writing – review & editing, Investigation, Resources.

Declaration of competing interest

The authors declare that they have no known competing financial interests or personal relationships that could have appeared to influence the work reported in this paper.

Data availability

Data will be made available on request.

Acknowledgments

This work is supported in part by the Carnegie Melon, USA through the Carnegie African Diaspora Fellowship Program, the National Science Foundation, USA (award No. DMR-220210) and National Research Foundation, South Africa (award No. 141942). Supercomputer and computational resources were provided by the Lehigh University High Performance Computing Center, and Center for High Performance Computing, Cape Town, South Africa.

Appendix A. Supplementary data

Supplementary material related to this article can be found online at https://doi.org/10.1016/j.surfin.2023.103091.

References

- [1] G.A. Prinz, Magnetoelectronics, Science 282 (5394) (1998) 1660–1663, http://dx.doi.org/10.1126/science.282.5394.1660, arXiv:https://www.science.org/doi/pdf/10.1126/science.282.5394.1660, URL https://www.science.org/doi/abs/10.1126/science.282.5394.1660.
- [2] J.M. Khalaf Al-zyadi, N.H. Abdul-Wahhab, K.-L. Yao, Half-metallicity of (001), (110) and (111) surfaces of zinc-blende mnbi and their interfaces with hgte: A first-principle investigation, J. Magn. Magn. Mater. 446 (2018) 221–230, http://dx.doi.org/10.1016/j.jmmm.2017.09.039, URL https://www.sciencedirect.com/science/article/pii/S0304885317322400.
- [3] J.M. Khalaf Al-zyadi, M.A. Nattiq, J.M. Al-Mukh, K.-L. Yao, Electronic structure and magnetic properties of the (001), (111) and (110) surfaces of scc with zinc blende structure, Solid State Commun. 314–315 (2020) 113941, http://dx.doi.org/10.1016/j.ssc.2020.113941, URL https://www.sciencedirect.com/ science/article/pii/S0038109820302659.
- [4] J.M. Khalaf Al-zyadi, H.I. Asker, K.-L. Yao, The half-metallic properties of bulk and the (111), (110) and (001) surfaces for the full heusler alloy zr2vin, Physica E 122 (2020) 114196, http://dx.doi.org/10.1016/j.physe.2020.114196, URL https://www.sciencedirect.com/science/article/pii/S1386947720304902.
- [5] J.M.K. Al-zyadi, A.H. Ati, K.-L. Yao, First-principles study of half-metallicity bulk rocksalt structure of cste and its surfaces, J. Electron Spectrosc. Relat. Phenom. 244 (2020) 146991, http://dx.doi.org/10.1016/j.elspec.2020.146991, URL https://www.sciencedirect.com/science/article/pii/S0368204820300591.
- [6] J.M.K. Al-zyadi, A.H. Ati, K.-L. Yao, Bulk and surfaces half-metallicity of rbse with zinc-blende structure: first-principles study, Appl. Phys. A 126 (2020) 1–7.

- [7] J.M. Khalaf Al-zyadi, H.I. Asker, A study half-metallic surfaces of the full-heusler sc2crge compound and the interface of sc2crge/insb (111), J. Electron Spectrosc. Relat. Phenom. 249 (2021) 147060, http://dx.doi.org/10. 1016/j.elspec.2021.147060, URL https://www.sciencedirect.com/science/article/ pii/S0368204821000189
- [8] R.A. de Groot, F.M. Mueller, P.G. v. Engen, K.H.J. Buschow, New class of materials: Half-metallic ferromagnets, Phys. Rev. Lett. 50 (1983) 2024– 2027, http://dx.doi.org/10.1103/PhysRevLett.50.2024, URL https://link.aps.org/ doi/10.1103/PhysRevLett.50.2024.
- [9] J. Lee, N. Sai, A.A. Demkov, Spin-polarized two-dimensional electron gas through electrostatic doping in *laalo*₃/euo heterostructures, Phys. Rev. B 82 (2010) 235305, http://dx.doi.org/10.1103/PhysRevB.82.235305, URL https://link.aps. org/doi/10.1103/PhysRevB.82.235305.
- [10] M. Kurahashi, X. Sun, Observation of a half-metallic interface state for pyridine-adsorbed h/fe3o4(100), J. Phys. Chem. Lett. 12 (35) (2021) 8489–8494, http://dx.doi.org/10.1021/acs.jpclett.1c02391.
- [11] S.O. Aisida, T.C. Chibueze, M.H. Alnasir, O.E. Oyewande, A. Raji, C. Ekuma, I. Ahmad, T. kai Zhao, M. Maaza, F.I. Ezema, Microstructural and magneto-optical properties of co1-xnix fe2o4 nanocomposites for hyperthermia applications, Solid State Sci. (2022) 107107, http://dx.doi.org/10.1016/j.solidstatesciences.2022.107107, URL https://www.sciencedirect.com/science/article/pii/S1293255822003028.
- [12] Y. Okimoto, T. Katsufuji, T. Ishikawa, A. Urushibara, T. Arima, Y. Tokura, Anomalous variation of optical spectra with spin polarization in double-exchange ferromagnet: la_{1-x}sr_xmno₃, Phys. Rev. Lett. 75 (1995) 109–112, http://dx.doi.org/10.1103/PhysRevLett.75.109, URL https://link.aps.org/doi/10.1103/PhysRevLett.75.109.
- [13] T.C. Chibueze, C.E. Ekuma, A.T. Raji, D.P. Rai, C.M.I. Okoye, Ferromagnetic half-metallicity in half-heusler aumnsn:te alloy, Mater. Res. Express 7 (7) (2020) 076519, http://dx.doi.org/10.1088/2053-1591/ab88ff.
- [14] T. Chibueze, A. Raji, C. Okoye, First principles study of the effects of doping with sp elements (as, sb, bi) and pressure on the properties of half-heusler aumnsn, Chem. Phys. 530 (2020) 110635, http://dx.doi.org/10.1016/j.chemphys.2019. 110635
- [15] Z. Cui, H. Ding, Y. Feng, Investigation of the half-metallicity, magnetism and spin transport properties of double half-heusler alloys mn2cocrz2 (z = p, as), Phys. Chem. Chem. Phys. 23 (2021) 17984–17991, http://dx.doi.org/10.1039/ D1CP01579F.
- [16] Lalrinkima, C.E. Ekuma, T.C. Chibueze, L.A. Fomin, I.V. Malikov, D. P. Rai L. Zadeng, Electronic, magnetic, vibrational, and x-ray spectroscopy of inverse full-heusler fe2irsi alloy, Phys. Chem. Chem. Phys. 23 (2021) 11876–11885, http://dx.doi.org/10.1039/D1CP00418B.
- [17] Y. Feng, H. Ding, B. Wu, Large magnetoresistance and temperature-driven spin filter effect in spin valve based on half Heusler alloy, J. Chem. Phys. 158 (11) (2023) 114706, http://dx.doi.org/10.1063/5.0124717, arXiv:https://pubs.aip.org/aip/jcp/article-pdf/doi/10.1063/5.0124717/16794717/114706_1.
- [18] T.C. Chibueze, C.E. Ekuma, A.T. Raji, F.I. Ezema, C.M.I. Okoye, Tetragonal and uniaxial strains in pristine and doped half-heusler aumnsn alloy, J. Alloys Compd. 848 (2020) 156186, http://dx.doi.org/10.1016/j.jallcom.2020.156186.
- [19] T.C. Chibueze, A.T. Raji, C.M.I. Okoye, Intrinsic point defects in half-heusler aumnsn, J. Phys. Chem. Solids 139 (2020) 109328, http://dx.doi.org/10.1016/ j.jpcs.2019.109328.
- [20] S.J. Hashemifar, P. Kratzer, M. Scheffler, Preserving the half-metallicity at the heusler alloy co₂MnSi(001) surface: A density functional theory study, Phys. Rev. Lett. 94 (2005) 096402, http://dx.doi.org/10.1103/PhysRevLett.94.096402, URL https://link.aps.org/doi/10.1103/PhysRevLett.94.096402.
- [21] B. Wu, H. Yuan, A. Kuang, H. Chen, Y. Feng, Appl. Surf. Sci. 258 (11) (2012) 4945–4951, http://dx.doi.org/10.1016/j.apsusc.2012.01.125, URL https://www.sciencedirect.com/science/article/pii/S0169433212001596.
- [22] Y. Hu, J.-M. Zhang, Thermodynamic stability, magnetism and half-metallicity of various (100) surfaces of heusler alloy ti2fesn, Mater. Chem. Phys. 192 (2017) 253–259, http://dx.doi.org/10.1016/j.matchemphys.2017.01.084, URL https:// www.sciencedirect.com/science/article/pii/S0254058417301219.
- [23] Y. Aharbil, H. Labrim, S. Benmokhtar, M.A. Haddouch, L. Bahmad, A. Belhaj, H. Ez-Zahraouy, A. Benyoussef, Ferromagnetism and half metallicity induced by oxygen vacancies in the double perovskite basrniwo6: Dft study, Mater. Chem. Phys. 183 (2016) 588–594, http://dx.doi.org/10.1016/j.matchemphys.2016.09.019, URL https://www.sciencedirect.com/science/article/pii/S0254058416306824.
- [24] S. Idrissi, S. Ziti, H. Labrim, L. Bahmad, Half-metallicity and magnetism in the full heusler alloy fe 2 mnsn with l21 and xa stability ordering phases, J. Low Temp. Phys. 202 (2021) 343–359.
- [25] M. Mouatassime, Y. Selmani, S. Idrissi, L. Bahmad, F. Goumrhar, H. Labrim, A. Benyoussef, Magnetic properties and half metallic behavior of the full-heusler co2fege alloy: Dft and monte carlo studies, J. Solid State Chem. 304 (2021) 122534, http://dx.doi.org/10.1016/j.jssc.2021.122534, URL https://www.sciencedirect.com/science/article/pii/S002245962100579X.
- [26] S. Idrissi, S. Ziti, H. Labrim, L. Bahmad, A. Benyoussef, Large curie temperature and robust half metallicity of the corhmnsi equiatomic quaternary heusler alloy, Ferroelectrics 582 (1) (2021) 36–45, http://dx.doi.org/10.1080/00150193.2021. 1951033.

- [27] H. Han, Z. Bai, K. Yao, Half-metallicity of bulk and (111) surface for full-heusler alloy co2val: A density functional study, J. Alloys Compd. 576 (2013) 93–97, http://dx.doi.org/10.1016/j.jallcom.2013.04.145, URL https:// www.sciencedirect.com/science/article/pii/S0925838813010669.
- [28] R. Paudel, J. Zhu, Investigation of half-metallicity and magnetism of bulk and (111)-surfaces of fe2mnp full heusler alloy, Vacuum 164 (2019) 336–342, http:// dx.doi.org/10.1016/j.vacuum.2019.03.049, URL https://www.sciencedirect.com/ science/article/pii/S0042207X19302775.
- [29] A. Dehghan, S. Davatolhagh, d0-d half-heusler alloys: A potential class of advanced spintronic materials, J. Alloys Compd. 772 (2019) 132–139, http:// dx.doi.org/10.1016/j.jallcom.2018.09.052, URL https://www.sciencedirect.com/ science/article/pii/S092583881833281X.
- [30] M. Rostami, M. Abedi, P. Amantorkaman, F. Kanjouri, Dft+u study of the bulk and (001), (110) and (111) surfaces of nacras half-heusler alloy with hydrogen adsorption for spintronics applications, Vacuum 175 (2020) 109278, http://dx.doi.org/10.1016/j.vacuum.2020.109278, URL https://www. sciencedirect.com/science/article/pii/S0042207X20301159.
- [31] D. Hoat, M. Naseri, R. Ponce-Pérez, J. Rivas-Silva, A. Kartamyshev, G.H. Cocoletzi, P-substitution effects on the electronic structure and thermal properties of the half-metallic half-heusler nacrbi compound, Chem. Phys. 537 (2020) 110848, http://dx.doi.org/10.1016/j.chemphys.2020.110848, URL https://www.sciencedirect.com/science/article/pii/S03011010420303797.
- [32] A. Dehghan, S. Davatolhagh, First principles study of d0-d half-heusler alloys containing group-iv, -v, and -vi sp atoms as prospective half-metals for real spintronic applications, Mater. Chem. Phys. 273 (2021) 125064, http://dx.doi.org/10.1016/j.matchemphys.2021.125064, URL https://www.sciencedirect.com/science/article/pii/S0254058421008476.
- [33] A. Jafari, S. Davatolhagh, A. Dehghan, Half-metallic p0-d half-heusler alloys with stable structure in ferromagnetic state, J. Phys. Chem. Solids 166 (2022) 110702, http://dx.doi.org/10.1016/j.jpcs.2022.110702.
- [34] S. Sanvito, C. Oses, J. Xue, A. Tiwari, M. Zic, T. Archer, P. Tozman, M. Venkatesan, M. Coey, S. Curtarolo, Accelerated discovery of new magnets in the heusler alloy family, Sci. Adv. 3 (4) (2017) e1602241, http://dx.doi.org/10.1126/sciadv.1602241, URL https://www.science.org/doi/abs/10.1126/sciadv.1602241.
- [35] T.T. Hoang, S.H. Rhim, S.C. Hong, Robust half-metallicities of alkali-metal-based half-heusler compounds, Phys. Rev. Mater. 6 (2022) 055001, http://dx.doi.org/10.1103/PhysRevMaterials.6.055001, URL https://link.aps.org/doi/10.1103/PhysRevMaterials.6.055001.
- [36] J.E. Fischer, J. Karel, S. Fabbrici, P. Adler, S. Ouardi, G.H. Fecher, F. Albertini, C. Felser, Magnetic properties and curie temperatures of disordered heusler compounds: co_{1+x}fe_{2-x}Si, Phys. Rev. B 94 (2016) 024418, http://dx.doi.org/10.1103/PhysRevB.94.024418, URL https://link.aps.org/doi/10.1103/PhysRevB.94.024418.
- [37] D. Rani, J. Kangsabanik, K.G. Suresh, N. Patra, D. Bhattacharyya, S.N. Jha, A. Alam, Origin of local atomic order and disorder in $co_2 fe_{1-x} cr_x Si$ heusler alloys: Theory and experiment, Phys. Rev. Appl. 10 (2018) 054022, http://dx.doi.org/10.1103/PhysRevApplied.10.054022, URL https://link.aps.org/doi/10.1103/PhysRevApplied.10.054022.
- [38] R. Mahat, U. Karki, S. KC, J.Y. Law, V. Franco, I. Galanakis, A. Gupta, P. LeClair, Effect of mixing the low-valence transition metal atoms y = co, fe, mn, cr, v, ti, or sc on the properties of quaternary heusler compounds co_{2-x}Y_xFeSi (0 ≤ x ≤ 1), Phys. Rev. Mater. 6 (2022) 064413, http://dx.doi.org/10.1103/PhysRevMaterials.6.064413, URL https://link.aps.org/doi/10.1103/PhysRevMaterials.6.064413.
- [39] M. Baral, V. Srihari, A. Bhakar, M.K. Chattopadhyay, P. Tiwari, A. Chakrabarti, T. Ganguli, Revealing superstructure ordering in co_{1+x}MnSb heusler alloys and its effect on structural, magnetic, and electronic properties, Phys. Rev. B 105 (2022) 184106, http://dx.doi.org/10.1103/PhysRevB.105.184106, URL https://link.aps.org/doi/10.1103/PhysRevB.105.184106.
- [40] Z. Dong, J. Luo, C. Wang, Y. Jiang, S. Tan, Y. Zhang, Y. Grin, Z. Yu, K. Guo, J. Zhang, W. Zhang, Half-heusler-like compounds with wide continuous compositions and tunable p-to n-type semiconducting thermoelectrics, Nature Commun. 13 (1) (2022) 1–9, http://dx.doi.org/10.1038/s41467-021-27795-3.
- [41] P. Hohenberg, W. Kohn, Inhomogeneous electron gas, Phys. Rev. 136 (1964) B864–B871, http://dx.doi.org/10.1103/PhysRev.136.B864, URL https://link.aps. org/doi/10.1103/PhysRev.136.B864.
- [42] W. Kohn, L.J. Sham, Self-consistent equations including exchange and correlation effects, Phys. Rev. 140 (1965) A1133–A1138, http://dx.doi.org/10.1103/PhysRev.140.A1133, URL https://link.aps.org/doi/10.1103/PhysRev.140.A1133.
- [43] P. Giannozzi, S. Baroni, N. Bonini, M. Calandra, R. Car, C. Cavazzoni, D. Ceresoli, G.L. Chiarotti, M. Cococcioni, I. Dabo, A.D. Corso, S. de Gironcoli, S. Fabris, G. Fratesi, R. Gebauer, U. Gerstmann, C. Gougoussis, A. Kokalj, M. Lazzeri, L. Martin-Samos, N. Marzari, F. Mauri, R. Mazzarello, S. Paolini, A. Pasquarello, L. Paulatto, C. Sbraccia, S. Scandolo, G. Sclauzero, A.P. Seitsonen, A. Smogunov, P. Umari, R.M. Wentzcovitch, Quantum espresso: a modular and open-source software project for quantum simulations of materials, J. Phys.: Condens. Matter 21 (39) (2009) 395502, http://dx.doi.org/10.1088/0953-8984/21/39/395502.
- [44] P. Giannozzi, O. Andreussi, T. Brumme, O. Bunau, M.B. Nardelli, M. Calandra, R. Car, C. Cavazzoni, D. Ceresoli, M. Cococcioni, N. Colonna, I. Carnimeo, A.D. Corso, S. de Gironcoli, P. Delugas, R.A. DiStasio, A. Ferretti, A. Floris, G. Fratesi,

- G. Fugallo, R. Gebauer, U. Gerstmann, F. Giustino, T. Gorni, J. Jia, M. Kawamura, H.-Y. Ko, A. Kokalj, E. Küçükbenli, M. Lazzeri, M. Marsili, N. Marzari, F. Mauri, N.L. Nguyen, H.-V. Nguyen, A.O. de-la Roza, L. Paulatto, S. Poncé, D. Rocca, R. Sabatini, B. Santra, M. Schlipf, A.P. Seitsonen, A. Smogunov, I. Timrov, T. Thonhauser, P. Umari, N. Vast, X. Wu, S. Baroni, Advanced capabilities for materials modelling with quantum espresso, J. Phys.: Condens. Matter 29 (46) (2017) 465901, http://dx.doi.org/10.1088/1361-648X/aa8f79.
- [45] J.P. Perdew, A. Ruzsinszky, G.I. Csonka, O.A. Vydrov, G.E. Scuseria, L.A. Constantin, X. Zhou, K. Burke, Restoring the density-gradient expansion for exchange in solids and surfaces, Phys. Rev. Lett. 100 (2008) 136406, http://dx.doi.org/10.1103/PhysRevLett.100.136406, URL https://link.aps.org/doi/10.1103/PhysRevLett.100.136406.
- [46] M. van Setten, M. Giantomassi, E. Bousquet, M. Verstraete, D. Hamann, X. Gonze, G.-M. Rignanese, The pseudodojo: Training and grading a 85 element optimized norm-conserving pseudopotential table, Comput. Phys. Comm. 226 (2018) 39–54, http://dx.doi.org/10.1016/j.cpc.2018.01.012, URL https://www.sciencedirect.com/science/article/pii/S0010465518300250.
- [47] H.J. Monkhorst, J.D. Pack, Special points for brillouin-zone integrations, Phys. Rev. B 13 (1976) 5188–5192, http://dx.doi.org/10.1103/PhysRevB.13.5188.
- [48] See Supplemental Material at [URL will be inserted by publisher]. The electronic density of states and atomic projected density of states of the evolution of strain-engineering in NaCrAs.
- [49] S. Baroni, P. Giannozzi, A. Testa, Green's-function approach to linear response in solids, Phys. Rev. Lett. 58 (1987) 1861–1864, http://dx.doi.org/10.1103/PhysRevLett.58.1861, URL https://link.aps.org/doi/10.1103/PhysRevLett.58.1861.
- [50] P. Giannozzi, S. de Gironcoli, P. Pavone, S. Baroni, Ab initio calculation of phonon dispersions in semiconductors, Phys. Rev. B 43 (1991) 7231–7242, http://dx.doi.org/10.1103/PhysRevB.43.7231, URL https://link.aps.org/doi/10. 1103/PhysRevB.43.7231.

- [51] J. Kübler, First principle theory of metallic magnetism, Physica B+C 127 (1) (1984) 257–263, http://dx.doi.org/10.1016/S0378-4363(84)80039-X, Proceedings of the 4th General Conference of the Condensed Matter Division of the EPS. URL https://www.sciencedirect.com/science/article/pii/S037843638480039X.
- [52] H. Ebert, D. Ködderitzsch, J. Minár, Calculating condensed matter properties using the kkr-green's function method—recent developments and applications, Rep. Progr. Phys. 74 (9) (2011) 096501, http://dx.doi.org/10.1088/0034-4885/ 74/9/096501.
- [53] H. Ebert, et al., The munich spr-kkr package, version 8.6, 2022, URL: https://www.ebert.cup.uni-muenchen.de/sprkkr.
- [54] P.W. Anderson, Theory of Magnetic Exchange Interactions: Exchange in Insulators and Semiconductors, in: Solid State Physics, vol. 14, Academic Press, 1963, pp. 99–214, http://dx.doi.org/10.1016/S0081-1947(08)60260-X, URL https://www.sciencedirect.com/science/article/pii/S008119470860260X.
- [55] S. Blundell, Magnetism in Condensed Matter, first ed., in: Oxford Maser Series in Condensed Matter Physics, Oxford University Press, USA, 2001, URL http: //gen.lib.rus.ec/book/index.php?md5=c4d8b9fbdb740f952e9b6a3761750172.
- [56] A. Liechtenstein, M. Katsnelson, V. Antropov, V. Gubanov, Local spin density functional approach to the theory of exchange interactions in ferromagnetic metals and alloys, J. Magn. Magn. Mater. 67 (1) (1987) 65–74, http://dx.doi.org/ 10.1016/0304-8853(87)90721-9, URL http://www.sciencedirect.com/science/ article/pii/0304885387907219.
- [57] K. Sato, W. Schweika, P.H. Dederichs, H. Katayama-Yoshida, Low-temperature ferromagnetism in (ga, mn)n: Ab initio calculations, Phys. Rev. B 70 (2004) 201202, http://dx.doi.org/10.1103/PhysRevB.70.201202, URL https://link.aps. org/doi/10.1103/PhysRevB.70.201202.
- [58] J. Zhang, X. Li, J. Yang, Electrical control of carriers' spin orientation in the fevtisi heusler alloy, J. Mater. Chem. C 3 (2015) 2563–2567, http://dx.doi.org/ 10.1039/C4TC02587C.
- [59] K. Reuter, M. Scheffler, Composition, structure, and stability of ruo₂(110) as a function of oxygen pressure, Phys. Rev. B 65 (2001) 035406, http://dx.doi.org/ 10.1103/PhysRevB.65.035406, URL https://link.aps.org/doi/10.1103/PhysRevB. 65.035406.